Minerals detection for hyperspectral images using adapted linear unmixing : LinMin

F. Schmidt, M. Legendre, S. Le Mouélic

To cite this version:

F. Schmidt, M. Legendre, S. Le Mouélic. Minerals detection for hyperspectral images using adapted linear unmixing : LinMin. Icarus, 2014, 237, pp.61-74 (IF 3,161). 10.1016/j.icarus.2014.03.044 . hal-01045080

HAL Id: hal-01045080
https://hal.science/hal-01045080v1

Submitted on 21 Mar 2024

Minerals detection for hyperspectral images using adapted linear unmixing: LinMin

Schmidt Frédéric[1,2], Maxime Legendre[3], Stéphane Le Mouëlic[4]

[1] *Univ Paris-Sud, Laboratoire IDES, UMR8148, Orsay, F-91405; (frederic.schmidt@u-psud.fr)* [2] *CNRS, Orsay, F-91405. Université Paris Sud* [3] *IRCCyN (CNRS UMR 6597), Ecole Centrale Nantes, France,* [4] *LPGN, CNRS UMR 6112, Université de Nantes, France*

Abstract

Minerals detection over large volume of spectra is the challenge addressed by current hyperspectral imaging spectrometer in Planetary Science. Instruments such OMEGA (Mars Express), CRISM (Mars Reconnaissance Orbiter), M^3 (Chandrayaan-1), VIRTIS (Rosetta) and many more, have been producing very large datasets since one decade. We propose here a fast supervised detection algorithm called LinMin, in the framework of linear unmixing, with innovative arrangement in order to treat non-linear cases due to radiative transfer in both atmosphere and surface. We use reference laboratory and synthetic spectral library. Additional spectra are used in order to mimic the effect of Martian aerosols, grain size, and observation geometry discrepancies between reference and observed spectra. The proposed algorithm estimates the uncertainty on "mixing coefficient" from the uncertainty of observed spectra. Both numerical and observational tests validate the approach. Fast parallel implementation of the best algorithm (IPLS) on Graphics Processing Units (GPU) allows to significantly reduce the computation cost by a factor of ˜40.

Keywords: spectroscopy, hyperspectral, supervised detection, linear unmixing under constraint, sum to one, positivity, GPU, LinMin

---

1. Introduction

Various methods have been proposed to detect surface chemical species (minerals, ice) on large dataset of hyperspectral images. Supervised methods (knowing the spectra of the chemical species you want to detect) are widely used, for instance : band ratio techniques ((Poulet et al., 2007; Ehlmann et al., 2011; Carter et al., 2013)), linear unmixing ((Combe et al., 2008; Themelis et al., 2012)), wavelet based detection ((Schmidt et al., 2007; Gendrin et al., 2006)), correlation based detection - Spectral Angle Mapper ((Kruse et al., 1993)). Other linear non-supervised techniques (estimating the spectra directly from the scene) have been proposed, using Independent Component Analysis ICA ((Forni et al., 2005; Erard et al., 2009)) or Bayesian methods under constrained ((Moussaoui et al., 2008; Schmidt et al., 2010)). Also some algorithms only extract the endmember spectra such: Pixel Purity Index ((Boardman et al., 1995)), N-FINDR ((Winter, 1999)), or graph-based segmentation ((Gilmore et al., 2011)) .

The linear mixture is still valid in non-linear intimate mixture, but with significant difference between retrieved "mixing coefficient" and actual abundance ((**?**Mustard et al., 1998)). Nevertheless, linear unmixing is satisfactory for mineral detection ((Combe et al., 2008; Themelis et al., 2012)). It has the significant advantage to deal with complex mixture of a large variety of candidate minerals (see fig. 3), whereas band ratio methods fails, due to the lack of defined reference "continuum" wavelength channel. In such situation each wavelength may sample an absorption band of a particular mineral and no reference wavelength can be found. If band ratio's are adapted to detect minerals over flat spectra, methods using the entire wavelength channels (such linear unmixing) are adapted to detect minerals over a complex variety of background. Specifically, we draw attention that the band ratio's of the CRISM summary products are only relevant in case of a pure mineral detection but may be irrelevant in case of a mixture. We propose here to address the challenge to detect one mineral type alone or a mineral type in an assemblage, from a very diverse potential endmember spectra dataset.

Linear unmixing is relatively simple enough to provide a fast implementation. Furthermore supervised linear unmixing has the advantage that its interpretation is directly and automatically provided in terms of mineralogical class on the bulk hyperspectral image. Dimensionality reduction methods, such unsupervised algorithms or endmember extractions are not required in linear unmixing. Also linear unmixing does not require manual interpretation and identification of spectra.

Previous linear unmixing algorithms have proposed to optimize the reference spectral library in order to solve positivity ((Combe et al., 2008)), forcing for sum-to-one constraints on the mixing coefficients ((Roberts et al., 1998)). (Roberts et al., 1998) discusses the benefits of constraining the number of endmembers from the spectral library. They have shown that the solutions with a mixture of two endmembers have less overlap that three endmembers mixtures, probably due to the dimension space. In our article, we focus on the interest of both positivity and sum-to-one constraints, that allow to estimate the optimum of all possibility of mixtures. Without positivity and sum-to-one constraints, singularities may arise due "linear dependance" of endmember spectra ((Roberts et al., 1998; Dalton et al., 2013)). We show that most recent algorithms, including both positivity and sum-to-one constraints, handle this difficulty, thus simplifying tremendously the treatment.

Our aim is to show that additional spectra (flat, slope) minimize the differences between reference laboratory spectra and actually observed spectra, by reducing the effect of grain size and continuum level (photometry, surface roughness, compaction). Some differences between observations and reference endmembers may still be present due to variations in composition, texture,...

The selection of the reference spectra database requires always special care and depends on the scientific questions addressed, but at least this database is explicitly known.

Once detection has been performed, time consuming inversions must be applied in order to retrieve quantitative estimate of surface properties (exact mineralogy, abundances, grain size, porosity, ...) as proposed by different techniques such MGM ((Sunshine and Pieters, 1993; Kanner et al., 2007)) or radiative transfer inversion ((Douté et al., 2007; Poulet et al., 2009a)). Also the particular mineral type, for instance Al/Fe or Mg/Fe phyllosilicate, must be addressed by additional work using specific spectral library.

We propose here to extend the linear supervised detection technique using a new set of constraint (positivity and sum to unity) and a new set of additional spectra in order to improve the "mixing coefficient" estimation. We also introduce a new renormalization with the goal to fit the signal, even in the case of very low signal to noise ratio.

We propose to call LinMin our strategy of using:

1. linear unmixing technique under constraints (positivity, sum to unity/sum lower than unity)
2. additional spectra made of flat and slope (also possibly cosine functions)
3. renormalization by the variance/covariance noise matrix
4. estimation of the error on the "mixing coefficient

In order to validate the LinMin approach, we test the detection limits on synthetic data simulating a regolith mixture, the grain size effect and the Martian aerosols effect. We also validate the method on actual hyperspectral dataset of OMEGA, CRISM and M^3. Quantitative estimate of the detection limits are computed.

2. Method

2.1. Linear unmixing

The linear mixing model of hyperspectral reflectance is usually written as:

$$X = A.S + E \tag{1}$$

with the collection of observed spectra X ($M \times N_\lambda$ matrix), the reference spectra S ($N \times N_\lambda$ matrix), the unknown mixing coefficients A ($M \times N$ matrix) and the additive noise error E ($M \times N_\lambda$ matrix), assumed to be gaussian with zero mean. N_λ is the number of wavelength, N the number of reference spectra, M the number of observed spectra.

The unmixing problem then consists in the estimation of the mixing coefficients A that minimize the error E. Considering the least squares error minimization, it is written:

$$\min_{A \in \Re^{M \times N}} F(A) \quad \text{with} \quad F(A) = \sum_{m=1}^{M} \sum_{\lambda=1}^{N_\lambda} (X_{m\lambda} - (A.S)_{m\lambda})^2 \tag{2}$$

The unconstrained solution $A = X.S^T.\left(S.S^T\right)^{-1}$ has been used the in previous detection methods ((Boardman et al., 1995; Combe et al., 2008)) but the retrieved mixing coefficient A may be negative. One solution is to test all combination of reference spectra S in order to keep only positive case ((Roberts et al., 1998; Combe et al., 2008)), but the computation cost is very high. In addition, such case is more sensitive to degeneracies in comparison to the constrained problem (see paragraph 2.4).

2.2. Linear unmixing under constraint

The previous formulation is not sufficient to describe physical constraints on the mixing coefficients. Indeed, the mixing coefficients must satisfy non-negativity :

$$\forall m \in \{1, \ldots, M\}\ \forall n \in \{1, \ldots, N\}\ A_{mn} \geq 0 \tag{3}$$

and sum-to-one constraints:

$$\forall m \in \{1, \ldots, M\}\ \sum_{n=1}^{N} A_{mn} = 1 \tag{4}$$

Non-Negative Least Squares (NNLS) algorithms((Lawson and Hanson, 1995; Bro and De Jong, 1997)) aim at solving the problem 2 subject to constraint 3. *Sum-to-one Constrained Least Squares* (SCLS) methods (Settle and Drake, 1993) solve the same problem with constraint 4. Eventually, *Fully Constrained Least Squares* (FCLS) algorithms ((Heinz and Chein-I-Chang, 2001; Dobigeon et al., 2008)) solve the problem 2 subject to both constraints 3 and 4. In this article, two FCLS methods are considered: (i) IPLS based on primal dual interior point optimization ((Chouzenoux et al., 2011)) that benefits from GPU implementation ((Chouzenoux et al., 2013)), (ii) BI-ICE in the bayesian framework ((Themelis et al., 2012)).

As stated in (Chouzenoux et al., 2013), the convexity of the criterion F is sufficient to establish the convergence of IPLS when constraints 3 and 4 are considered. Hence, the unmixing estimation can be performed even with correlated reference spectra, such in fig. 2. Next sections will describe the results on actual data.

2.3. Measurement uncertainty consideration

In some cases, the level of uncertainty is known and can be modeled by a gaussian probability density function with zero mean and the covariance C ($N_\lambda \times N_\lambda$ matrix). C^{-1} being a symmetric positive definite matrix, it can be factorized using the Cholesky decomposition:

$$C^{-1} = L.L^T \tag{5}$$

with L lower triangular. Thus, noting $X = [X_1, \ldots, X_M]^T$ and $A = [A_1, \ldots, A_M]^T$, the least squares criterion becomes:

$$\min_{A \in \Re^{M \times N}} F(A) \quad \text{with} \quad F(A) = \sum_{m=1}^{M} (X'_m - A_m.S')(X'_m - A_m.S')^T \tag{6}$$

with $X' = X.L$ and $S' = S.L$. Thereby, the measurement uncertainty is handled by modifying the observation matrix X and the reference spectra S before the unmixing process.

An estimation of the error on the mixing coefficient A is directly provided by the Hessian ((Chouzenoux et al., 2013)).

2.4. Reference spectra database

As stated in introduction, the reference spectra database depends on the scientific goal of the detection. The total number of spectra is limited to the number of wavelength. In the following, we used 32 spectra of the main minerals type proposed to be present at the surface of Mars and the Moon (see fig. 3). More endmembers can be used but with increasing computation time ((Chouzenoux et al., 2013)).

The linear unmixing problem (eq. 2) is degenerated if the spectra in the database are linearly dependent. Degeneracies can create false solution with low RMS error ((Roberts et al., 1998; Combe et al., 2008)). We estimate here the linear dependence of the database in order to show that positivity constraint significantly decreases the appearance of degeneracies. This test is an "autofit" of the reference spectra database. For each spectra of the database S_n, we estimate the abundance matrix A', for a new set of reference spectra made of all endmembers except S_n ($S' = S \setminus S_n$). We use the unconstrained problem (eq. 2):

$$S_n = A'.S' + E \tag{7}$$

and also the non-negative constrained problem (eq. 2 subject to constraint 3) to estimate A'.

Figure 1, shows the residue E between the real endmember S_n and the best linear mixture of all other endmember $A'.S'$, for all endmembers. The unconstrained problem shows smaller residues than the positivity constrained problem. In addition, the residues are unstructured (noisy) for the unconstrained problem, in contradiction to the very structured residues (inverted spectra) for the positivity constrained problem. This fact indicates that the spectra $S_n - E$ is better fitted with a linear mixture of false endmember S'instead of the real case. In conclusion, an observed spectra with noise can likely create false detection in the unconstrained problem but much less likely in the positivity constrained problem.

2.5. Benefits of additional spectra

In order to model the effect of shading, grain size and aerosols, (Combe et al., 2008) propose to add a positive and a negative linear slope, and also a

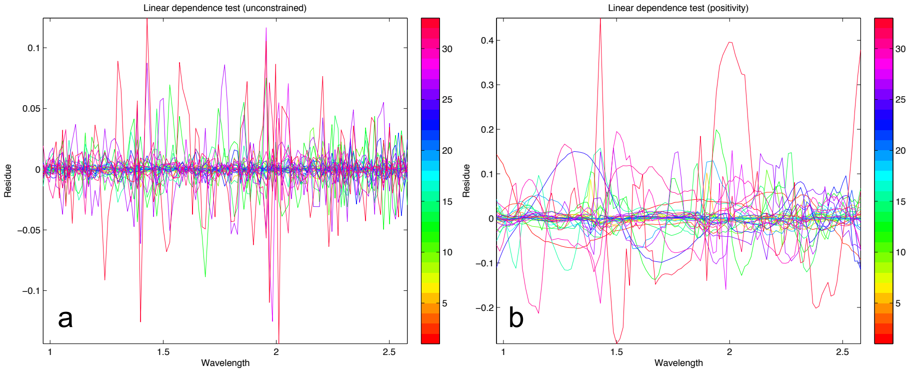

Figure 1: Estimation of degeneracies of the reference database: (a) on left without positivity constraints, (b) on right with positivity constraints.

flat spectrum in order to correct for the Mie scattering of the aerosols particles (see fig. 2 in (Combe et al., 2008)).

This strategy can be extended in the case of linear unmixing under constraints. Since mixing coefficients are positive and constrained to one, the flat spectra split in two : flat near zero level and also near 1 level (see fig. 2). Those 4 additional spectra allows to model the difference of level and slope between X and S.

In order to model more complex continuum shape such aerosols, we could also add cosine function with periods x2 and x4 of the spectral domain ((Schmidt et al., 2011, 2012)). Similarly to Fourier transform, those cosine functions are orthogonal and linearly independent, allowing unique mixing coefficient. In the framework of linear unmixing under positivity and sum to one constraint, 12 additional spectra are required. Those 12 additional spectra allow to model the large scale difference between X and S, similar to Fourier filtering. In particular the aerosols contribution that peak at the wavelength similar to the grain size may be fitted by large scale cosine. Figure 5 (b) show a pure aerosol spectra (aot=100), that could be modeled by level/slope/sine/cosine functions. Since the aerosols grain size may change, leading to an unknown peak over the wavelength, our approach will be able to fit it.

Since those 4 (or 12) additional spectra are highly correlated, from algorithmic point of view it may hard to estimate the mixing coefficient. To our knowledge, the only algorithms that are able to estimate the unmixing under constraints and high correlated reference spectra are IPLS ((Chouzenoux et al., 2011)) and BI-ICE ((Themelis et al., 2012)). Next section will describe the results on actual data.

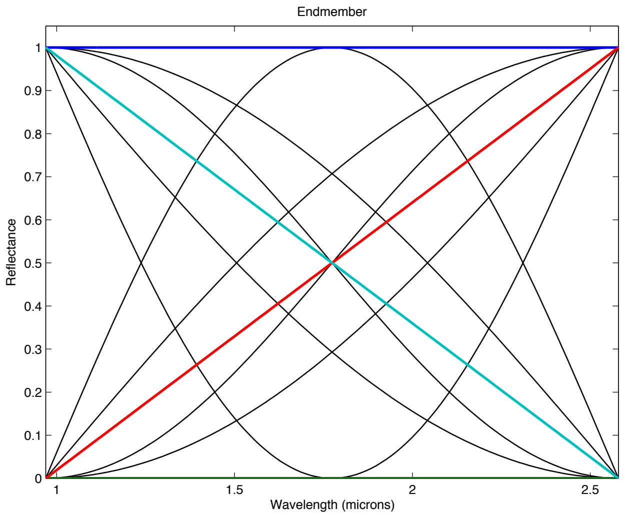

Figure 2: thick color lines : 4 additional spectra to fit difference of level and slope between X and S. thin black lines : 8 cosine/sine function to model the large scale difference between X and S.

3. Synthetic tests

In order to test the effect of various discrepancies between observation and reference spectra on detection accuracy, we propose to simulate 3 cases: linear random mixture at the surface without atmosphere, linear random mixture at the surface observed trough a diffusive atmosphere, grain size change.

3.1. Surface mixture

In order to simulate a realistic set of spectra, we create a random set of 1000 binary mixture spectra from our 32 reference spectra database (see fig. 3) from USGS catalog ((Clark et al., 2003)), the CRISM Analysis Tool (CAT), synthetic spectra from radiative transfer model ((Douté and Schmitt, 1998)). Each simulated spectra are composed of:

- 90% is a flat component at reflectance 0.35 in agreement with OMEGA studies (Vincendon, 2013) in order to reproduce the low level and flatness of actual Martian spectra. The flatness is also representative of the Moon or other planetary surface.
- 10% of a random mixture of two over 32 reference spectra with random uniform mixing coefficients, noted as A_0. For each endmember i, there is ˜30 spectral mixture with non-null mixing coefficient (noted $A^{positive}$) and ˜970 with null mixing coefficient (A^{false}).

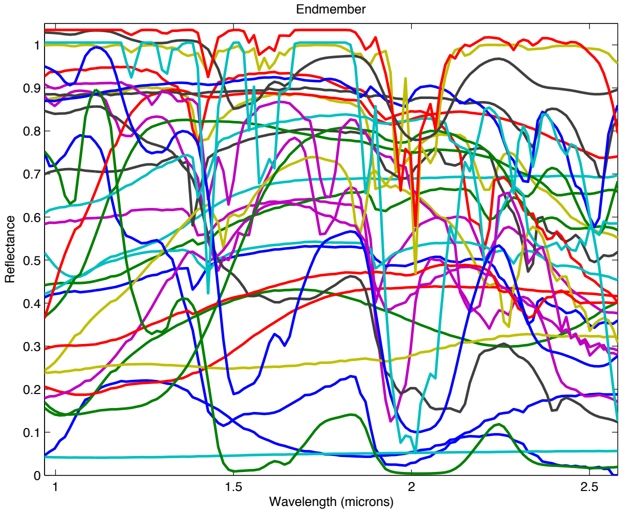

Figure 3: 32 Reference spectra of minerals, ice and atmospheric gas representing major classes of contributions of surface spectra. The difficulty to define continuum wavelength is due to the overlapping signatures of all species. See Appendix for the names.

We add synthetic noise, simulating the noise level of a typical OMEGA observation after gas correction. We estimate the noise covariance matrix from dark current noise of ORB41_1, transferred into the gas corrected calibrated observation space. The noise has a wavelength-average standard deviation of 1.3×10^{-3}. Other noise statistics can be used, such MNF shift difference from ENVI software, but we point the fact that OMEGA dark current is archived, estimating the minimum noise statistics (excluding spike and other non-linear effects).

The estimated mixing coefficients are noted A_{IPLS}, A_{BI-ICE} and $A_{IPLS,cov}$ for the renormalized problem.

Examples of fits are shown in fig. 5 on left with AOT=0.

Figure 4 compares estimated $A_{IPLS,cov}$ and actual A_0 mixing coefficients, for the IPLS algorithm using 32 and the 4 additional spectra, on the 1000 binary mixture, with the renormalized unmixing problem. Usually, $A_{IPLS,cov}$ for actually present endmember ($A_{IPLS,cov}^{positive}$ in green), are well separated from the absent endmember ($A_{IPLS,cov}^{false}$ in red), showing that a simple threshold can be used to detect the endmember. Endmember No 18 (Magnetite) is not detectable because there is no difference between $A_{IPLS,cov}^{positive}$ and $A_{IPLS,cov}^{false}$. Please note that $A_{IPLS,cov}^{positive}$ and $A_0^{positive}$ are very close, the mean absolute difference is 0.0142, one order of magnitude lower than the mixing coefficients (up to 10%), showing that when linear mixing is true, the estimated mixing coefficients are validated as real abundances. Also, the root-mean-square (RMS) error is compatible with the level of noise (1.2×10^{-3}).

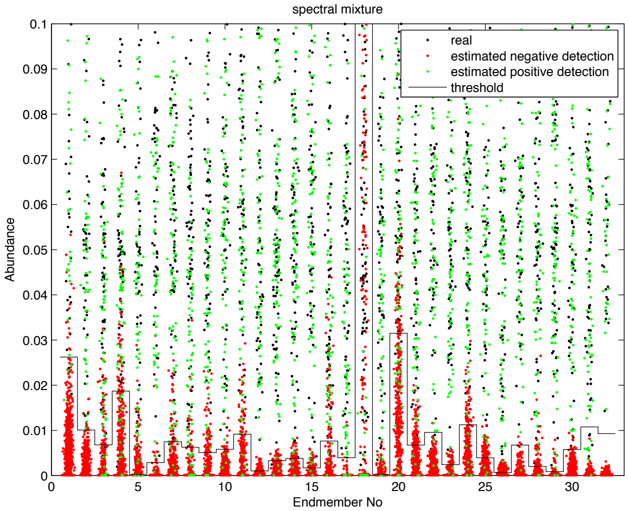

Figure 4: Mixing coefficient for 32 spectra (see fig. 3) for the IPLS algorithm on 1000 binary mixture, solving the renormalized unmixing problem (eq. 6), using 36 endmembers (32 spectra and the 4 additional spectra). black points: actual mixing coefficient A_0, generated randomly. green points: estimated mixing coefficient $A_{IPLS,cov}^{positive}$ in the case of positive detection. red points: estimated mixing coefficient $A_{IPLS,cov}^{false}$ in the case of false detection. black line: best threshold $C_{IPLS,cov}^{i}$ to detect the endmember. Please note that artificial dispersion around the endmember No has been added in order to increase the clarity of the figure.

In order to estimate the best threshold $C^i_{IPLS,cov}$, avoiding the maximum number of false detection but keeping the maximum positive detection, we propose the following formulation, for each endmember i:

$$C^i_{IPLS,cov} = \frac{1}{2}\left(mean(A^{positive}_{IPLS,cov}) - 2.std(A^{positive}_{IPLS,cov}) + mean(A^{false}_{IPLS,cov}) + 6.std(A^{false}_{IPLS,cov})\right) \tag{8}$$

Figure 4 shows these threshold for all endmembers. It confirms that some endmembers can be detected with a larger detection limits than other, depending on their relative similarities. Endmember No 18 (Magnetite) is not detectable because its spectral shape is too close to a combination of the 4 artificial spectra, because its spectra is featureless.

Actual positive detection and false detection rates without atmosphere are shown in figure 7 at the AOT=10^{-3} for IPLS with/without renormalization, for IPLS and BI-ICE, for 32 or 36 or 44 endmembers. For all algorithms the 4 additional spectra (called slope), clearly improve the classification over the 32 endmembers case (called no slope). Without renormalization, IPLS shows the best results ($>$ 70% of positive detection, $<$ 20% of false detection) over BI-ICE. With renormalization, the detection rates is improved ($>$ 85% of positive detection, $<$ 5% of false detection) for IPLS. For non-renormalized IPLS, the sum-to-one (sto) seems slightly better than sum-lower-than-one (slo).

The use of 12 additional spectra (including the sine/cosine), seems to be less efficient that 4 additional spectra (83 % of positive detection, 5% of false detection). It appears that the accuracy of detection slightly decreases for some minerals with large scale feature such olivines or pyroxenes. Since, those phases are major ones, we decide to focus on the 4 additional spectra.

As a summary, the best algorithm to detect linear mixture is clearly IPLS with renormalization and 4 additional spectra. Please note that a different threshold may change the positive/false detection rates but not change the relative accuracy of the classification. Estimating the threshold for real case images is more difficult due to the possible differences between observation and reference spectra. Please note that our test uses the same spectra in the spectral library and in the mixture.

3.2. Aerosols

In order to test if our methodology is able to reduce the effect of the non linear surface-atmosphere coupling due to aerosols, we modified the previous surface spectra by non linear radiative transfer using aerosol properties from (Vincendon et al., 2007). These authors propose a parameterization of the dust aerosol properties in form of a single scattering albedo and a shape of optical thickness as a function of wavelength, rescaled to a Aerosols Optical Thickness at 1 micron (AOT). The reflectance of a semi-infinite aerosol media is plotted in figure 5 b, for AOT=100. The simulation uses the DISORT algorithm ((Stamnes et al., 1988)) with the bottom condition as lambertian surface with the previous surface mixture spectra. We took into account the reflection and absorption of the aerosols but also the multiple reflection between surface and atmosphere. We used the following geometry, typical of hyperspectral observation: emergence angle 0°, incidence angle 76°, azimuth angle 60°. Other optical properties and/or geometries may be used but we assume that the chosen properties are reasonable to simulate aerosols effects. We sample 104 values of AOT (Aerosols Optical Thickness):

- The value 0 for no aerosols, identical to surface only (noted 10^{-3} in the log scale graphs)
- 99 value in a logarithm from 0.01 to 4.6 using $-\log(\frac{100-[1:99]}{100})$.
- Four values : 5, 10, 20 and 100 to sample the optically thick cases.

We obtain a set of 104 000 spectra simulating the space-borne Martian observation from the top of the atmosphere. We also add the synthetic OMEGA noise in order to simulate a realistic observation using the same approach that previously described.

On a desktop with Dual Core at 2.53 Ghz with 4Go RAM memory, the typical computation time to solve the non-normalized problem of eq. 2 on $M = 104000$ spectra with $N_\lambda = 110$, $N = 36$ are : 3.3 h for BI-ICE, 4.5 min for IPLS. The estimated mixing coefficients are noted A_{IPLS}, A_{BI-ICE}. Since IPLS is the fastest algorithm, we also tried the solve the harder renormalized problem of eq. 6 and found a computation time of 1.2h. We also use IPLS to solve the renormalized problem using 12 additional spectra. The estimated mixing coefficients are noted $A_{IPLS,cov}$. Also GPU implementation on a TESLA C 2050 (448 core at 1.15 GHz) may solve the problem with a computation time of several 10s. The GPU implementation efficiency dependance on spectral/spatial size and number of endmember is discussed in (Chouzenoux et al., 2013).

In order to illustrate the effect of AOT on the detection limits, figure 6 shows the same than figure 4 but for AOT=1. The positive detection mixing coefficients endmembers ($A^{positive}_{IPLS,cov}$ in green) are well separated from the absent endmember ($A^{false}_{IPLS,cov}$ in red), showing again that a simple threshold can be used to detect the endmember. Endmember No 18 (Magnetite) is still not detectable. Please note that $A^{positive}_{IPLS,cov}$ and $A^{positive}_{0}$ are getting far, the mean absolute difference is 0.0310, showing that when linear mixing is not true, the estimated mixing coefficient may differ from the true abundances. The estimated mixing coefficients $A^{positive}_{IPLS,cov}$ are systematically lower than the “true” $A^{positive}_{0}$ because of the effect of aerosols, removing the minerals signature (see fig. 5).

Results on actual positive detection and false detection rates are shown in figure 7 as a function of AOT. The positive detection rates of all algorithms drop for AOT$> 10^{-1}$. For IPLS with renormalization, the positive detection rates is 70 % at AOT=10^0 and 10 % at AOT=10^1, showing again that it is the best algorithm. IPLS with renormalization is also the only providing a constant low false detection rate (<5 %), independent of the AOT. The RMS error for IPLS with renormalization and additional spectra is still very low and compatible with the actual level of noise (at maximum 1.7×10^{-3} for AOT=10^2), showing that the non-linearity of the radiative transfer due aerosols can be fitted with our model. Examples of fits are shown in fig. 5 b) demonstrating the effect of decreasing mixing coefficient as a function of increasing AOT.

Figures 5 c) and d) show the effect of 4 additional spectra (level and slope) or 12 additional spectra (level, slope, cosine) on the detection of pure diopside. In the case of AOT=1 using 12 additional spectra, the mixing coefficient is estimated to be $0.7 \pm 2\%$, showing a non-probable detection in spite of the actual 10% abundance. In the same case using 4 additional spectra, the mixing coefficient is estimated to $5.5 \pm 0.2\%$, showing a clear positive good detection. We argue that all endmember with large scale absorption bands could have the same behavior and thus, we prefer to use 4 additional spectra to detect them. Users focused on spectra endmember with small scale features only, such phyllosilicate, could use the 12 additional spectra.

As a summary, the best algorithm to detect non-linear coupling of a linear mixture under increasing aerosols content is IPLS with renormalization and additional spectra. Please note that a different threshold may change the positive/false detection rates but not change the relative accuracy of the classification. Estimating the threshold for real case images is more difficult due to the possible differences between observation and reference spectra. Please note that our test uses the same spectra in the spectral library and in the mixture.

Comparison with band ratio. In order to estimate the accuracy of those results with the mostly used technique: band ratio, we compute the 1 microns band spectral parameter to detect forsterite ((Poulet et al., 2007; Ody et al., 2013)), called OSP1 ((Ody et al., 2013)), in our dataset. Figure 8 a) presents the pure endmember with a ratio greater than the defined threshold (1.04) ((Poulet et al., 2007; Ody et al., 2013)). This result shows the phenomena of false detection that could occur in the presence of other endmembers, indicating that band ratio is relevant to detect the presence of one single mineral feature vs no feature but it is not able to handle detect mineral against a large dataset of mineral. This is due to the difficulty to define a “continuum” wavelength, as shown in figure 3.

Figure 8 b) presents the detection of forsterite of the 1000 synthetic examples as a function of AOT, for the OSP1 band ratio and IPLS with different constraints. The band ratio seems to be have difficulties to detect the presence of forsterite in the 71 cases of mixture, because only 5% are detected. IPLS is able to detect up to 60% of the mixture with forsterite with the use of additional spectra, with a small range of false detection (<5%), similar to OSP1. In the case of IPLS without additional spectra, the false detection rate is very large (˜20%) and independent of the AOT, indicating wrong results. In this case, IPLS performs a better detection with additional spectra.

As a summary, in case of diverse spectra and mixture, one single band ratio is not able to detect the current spectra. This difficulty may be tackled by defining several band ratios but it is more difficult with an increasing number of candidate spectra. The LinMin strategy performs significantly better with additional spectra.

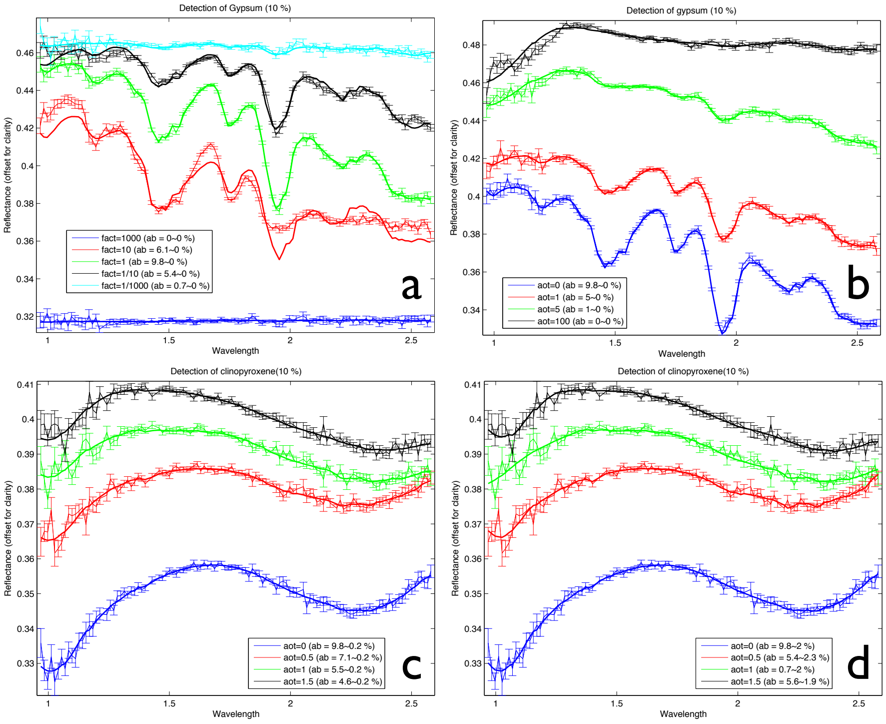

Figure 5: Examples of results using the IPLS algorithm: a) and b) with renormalization and 12 additional spectra (flat and slope) in the case of a pure gypsum spectra (10% in abundance). a) with different grain size factor, from x1000 to x1/1000, b) with different atmospheric load from AOT=0 to AOT=100. ; c) and d) with renormalization in the case of diopside (clinopyroxene). c) using 4 additional spectra (flat and slope), d) using 12 additional spectra (flat, slope and cosine).

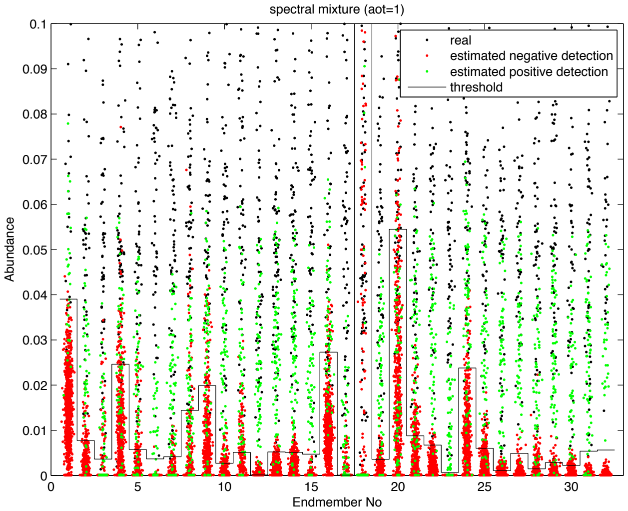

Figure 6: Same fig. as 4 but with AOT=1 instead of AOT=0.

3.3. Grain size

We choose the first 26 minerals spectra (see Appendix) with following parameter to retrieve the optical index of the grain material using the inverse Shkuratov theory ((Shkuratov et al., 1999)): real optical constant=1.7, volume fraction filled by particles=0.8, grain size=100 microns. This approach has been widely used in hyperspectral data analysis ((Poulet et al., 2002; Douté et al., 2007; Poulet et al., 2009b)).

We then regenerate the reflectance spectra using the direct Shkuratov theory but with 9 different grain size factor x1000, x100, x10, x5, x1, x$\frac{1}{5}$, x$\frac{1}{10}$, x$\frac{1}{100}$, x$\frac{1}{1000}$ of the original 100 microns. We obtain a set of 234 synthetic spectra.

In order to simulate a realistic observation we use the same approach that previously described for the surface mixture using flattening of the spectra and OMEGA noise addition (see section 3.1).

We do not claim that all reference spectra have been recorded at a grain size of 100 microns so that the generated dataset has a determined accurate grain size. Nevertheless, this manner allows us to generate synthetic spectra simulating a grain size factor change.

Since IPLS with renormalization is obviously the best algorithm, we only tested this approach for the grain size. We used again the same threshold strategy explained earlier in eq. 8. Here positivity constraint only may be relevant in the case of higher grain size than the endmember, since the signature are stronger and may imply mixing coefficient larger than 1.

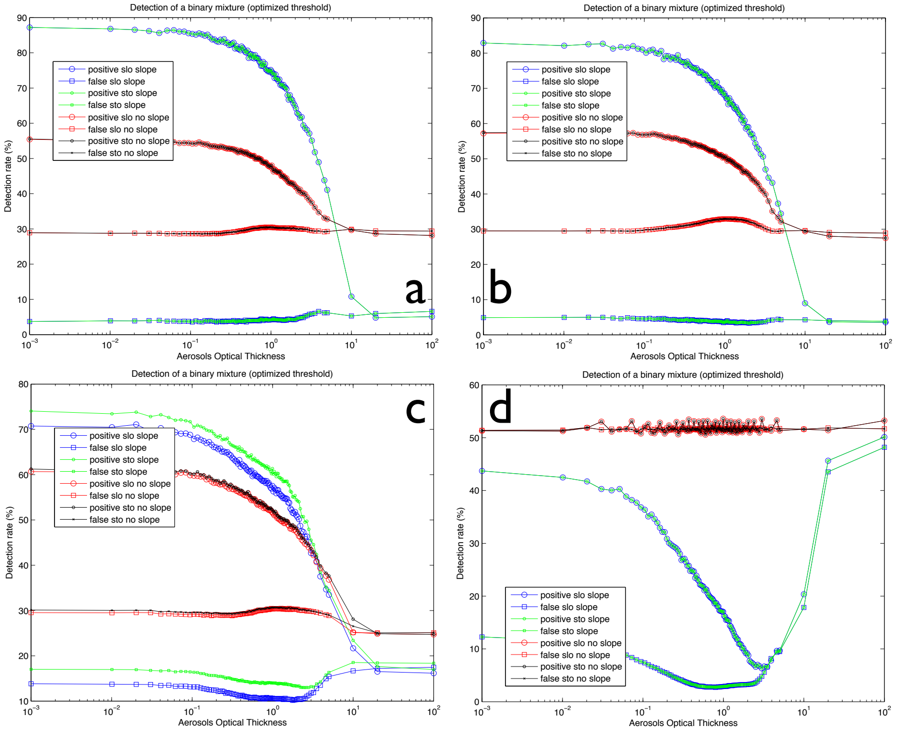

Figure 7: Positive detection rate (circle) and false detection rates (square) with optimized threshold as a function of AOT for (a) IPLS with renormalization and 36 endmembers (b) IPLS with renormalization and 44 endmembers (c), IPLS without renormalization and 36 endmembers (d) BI-ICE without renormalization and 36 endmembers. For each algorithm, the positive/false detection rates are computed using 32 endmember spectra only (no slope), or 36/44 endmember spectra (slope). IPLS has an option of sum-lower-than-one (slo) or sum-to-one (sto) that is not relevant for other algorithms. The case without aerosols is plotted at AOT=10^{-3}.

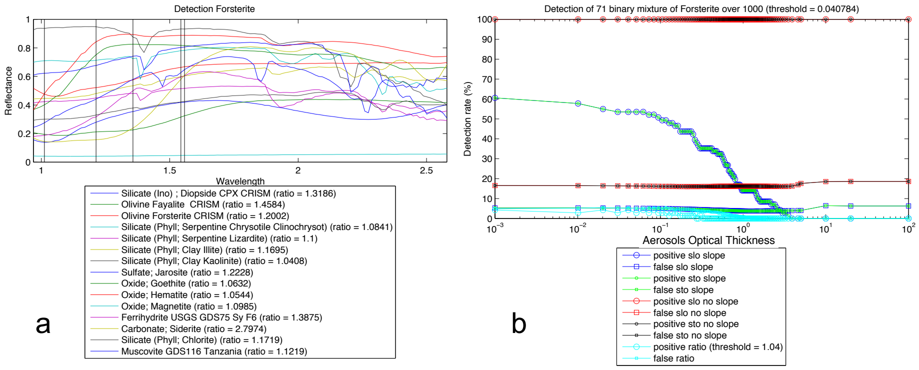

Figure 8: Detection of forsterite using band ratio and LinMin strategy using IPLS with renormalization and 44 endmembers. Only 71 mixtures over 1000 contains forsterite. (a) Detection rates and false detection rates as a function of AOT (b) random examples of false detection using band ratio (>1.04), but absence of detection with LinMin (mixing coefficient $\sim 10^{-5}$)

Positive and negative detection rates are plotted in fig. 9 for 36 or 32 spectra, for three constraints of IPLS : sum-lower-than-one (slo), sum-to-one (sto) and positivity only (pos). First of all, the detection is nearly perfect (>90%) for the grain size factor of x1, x5 and x1/5 using additional 4 spectra. The false detection rate is very low (<2%). For 32 spectra, the positive detection is around 60% for factor x1 to x10, and false detection is around 20%. Using the 4 additional spectra clearly improves the detection rates but slo, sto and pos are equivalent in this case. For a factor of x$\frac{1}{10}$ to x10, the detection rate is higher than 65%. It then decreases, moving away from factor x1. The detection rates are quite symmetrical in respect to increasing and decreasing grain size, with a slightly lower detection rates for the increasing grain size. Examples of fits are shown in fig. 5 demonstrating the effect of decreasing mixing coefficient as a function of increasing/decreasing grain size factor. This plot clearly shows that increasing grain sizes are more difficult to handle with our strategy because the error between estimated spectra and true one is higher. The main solution is to provide the endmembers with grain size higher than expected.

The RMS error is still very low and compatible with the actual level of noise (at maximum 2.1×10^{-3}), showing that the main non-linearity effects due grain size factor can be fitted with our model.

As a summary, the best endmembers to detect mineral species in case of a non-linear grain size effect again with the 4 additional spectra. Please note that a different threshold may change the positive/false detection rates but not change the relative accuracy of the classification. Estimating the threshold for real case images is more difficult due to the possible differences between observation and reference spectra. Please note that our test uses the same spectra in the spectral library and in the mixture. Intimate mixture may be generated from the Shkuratov theory but the detection limits may be forecast

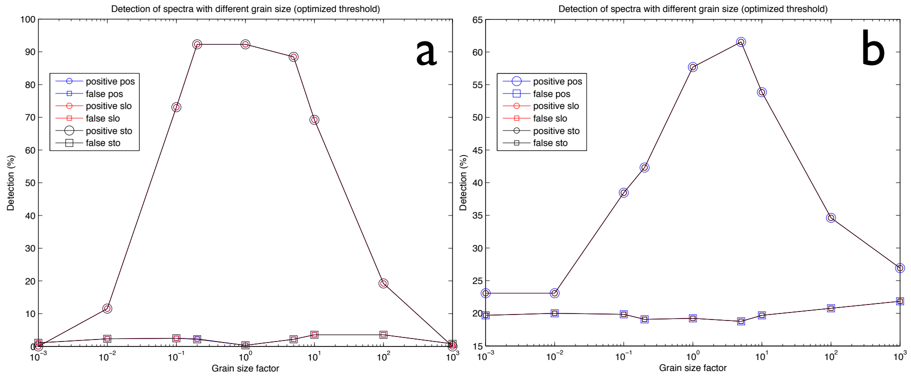

Figure 9: Positive detection rate (circle) and false detection rates (square) with optimized threshold as a function of grain size factor for IPLS with renormalization: (a) using 36 endmember spectra (using additional flat and slope endmember), (b) using 32 endmember spectra only (no slope). IPLS has options of constraints: sum-lower-than-one (slo), sum-to-one (sto) and positivity only (pos).

from this discussion, knowing that the largest grain size species is spectrally dominant (as computed for ices in (Schmidt et al., 2007) for instance).

4. Real case

We propose to test our automatic algorithm to three different real case from OMEGA, CRISM and M^3 instrument. For all cases, we will compare our results with other detection from the literature, mainly based on band ratio followed by ratio of the region of interest spectra over a manually selected “flat” spectra. For all cases, we do not test that the exact minerals types could be detected since many equivalent spectra can be identified (clays, olivine, pyroxene, ...). The names are the names of the material from laboratory spectra. For instance “goethite” is an example of iron oxide. Since all mineral inside a class are spectrally close (like for iron-oxides), it may be not possible to distinguish the precise mineral. We decided to keep magnetite since it has been detected on Mars ((Chevrier and Mathe, 2007)) but estimated mixing coefficients are not relevant due to the featureless spectra. More accurate detections are possible by adapting and improving the endmember spectra database. All maps, spectral fits of the maximum mixing coefficient and average of each compounds are available in supplementary material.

From previous section, IPLS seems the best algorithm to solve the LinMin problem so that we will exclusively use it on the real case hyperspectral images.

The detection of minerals requires different conditions of good behavior of the solution:

- The maximum mixing coefficient of the mineral should be higher than a certain threshold. This condition permits to focus on the main spectral component but component with smaller contribution can be present. We define the best compromise threshold for each observation due to noise level uncertainties.

- The error on mixing coefficient should be lower than the mixing coefficient, in order to have a significant detection.
- The RMS should be lower than the noise, basically estimated at 10 times the dark current noise.

4.1. OMEGA

We select the observation ORB422_4 of Observatoire pour la Minéralogie, l'Eau, les Glaces et l'Activité (OMEGA) onboard Mars Express (MEx) ((Bibring et al., 2004)) of Syrtis Major as a test case because this single cube contains well identified areas with very strong signatures of mafic minerals (pyroxenes, olivines) and phyllosilicates ((Mustard et al., 2005; Combe et al., 2008; Ehlmann and Mustard, 2012)). The data cube has been radiometrically calibrated and the atmospheric gas transmission has been empirically corrected using the volcano scan method ((Erard and Calvin, 1997; Langevin et al., 2005)). We estimated the noise covariance matrix on the calibrated and atmosphere corrected cube from the dark current. We then applied the renormalized IPLS algorithm using 36 spectra and sum-lower-than-one constraint.

The mixing coefficient results, plotted in figure 10, shows that orthopyroxene, clinopyroxene, olivine, goethite, clays and maghemite are detected, in agreement with previous detection ((Mustard et al., 2005; Combe et al., 2008; Ehlmann and Mustard, 2012)). The fit of the spectra with highest mixing coefficient are available in supplementary material. The estimated noise standard deviation is 3.3×10^{-4} from dark current but 5.0×10^{-3} using the MNF shift difference from ENVI software. The lack of fit estimated by the RMS error is 2.1×10^{-3} , in agreement with the previous two extreme values. Using the fast GPU implementation, the computation time is only 4 minutes for the complete OMEGA image of M =128x366 pixels, $N_\lambda = 110$ bands. The computation time can can be reduced to 0.3 min without any significant change in case of a recalibration with $C \times 100$.

4.2. CRISM

We propose to use the Compact Reconnaissance Imaging Spectrometer for Mars (CRISM) onboard Mars Reconnaissance Orbiter (MRO) image frt0000A09C ((Murchie et al., 2007)) of Nili Fossae where carbonate has been detected using manual band ratio's technique on stacked denoise spectra, divided by a spectrally flat component ((Ehlmann et al., 2009)). The data cube has been radiometrically calibrated and the atmospheric gas transmission has been empirically corrected using the volcano scan method ((McGuire et al., 2008)). We estimate the noise covariance matrix with the SNR=400 from the calibration at the ground ((Murchie et al., 2007)) in the diagonal elements. We also add a component in the non-diagonal terms of the covariance matrix in order to

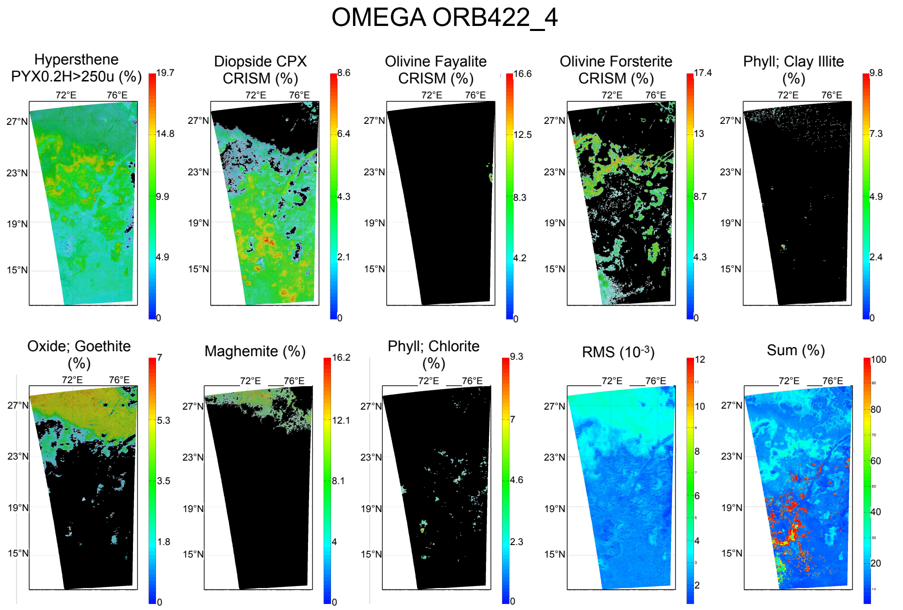

Figure 10: Detection of 8 minerals over 36 spectra on OMEGA image ORB422_4 of Syrtis Major using IPLS in the hue-saturation-value color system. The hue (color) represents the mixing coefficient. The saturation (color or b/w) represents the error. The value (intensity of color or b/w) represents the rms. Spectral mixing coefficient map are shown with following conditions : (i) maximum mixing coefficient $> 5\%$, (ii) error on mixing coefficient $<$ mixing coefficient, and (iii) RMS $<$ 10x the dark current noise (see text). Pyroxenes, olivines, phyllosilicates and oxides are detected and the corresponding “mixing coefficient“ are mapped (color refer to the online version of the article).

take into account the correlation of the bands due to atmospheric gas residuals. We corrected for the striped noise by removing the small scale residual in each column ((Parente, 2008)). Nevertheless, this method is not able to fully remove the non-gaussian noise and other more sophisticated methods could be applied ((Parente, 2008; Carter et al., 2013)). We did not correct for spectral smile ((Murchie et al., 2007)) unless this artifact can be corrected ((Ceamanos and Doute, 2010)). Since the algorithm is comparing observed spectra to a single reference spectra that cannot be shifted in wavelength, results may be affected by the smile artifact. Nevertheless, the absorption bands of minerals are often large and very insensitive to spectral smile, which is not the case for gas and ices. Band ratios techniques may be less sensitive to spectral smile for detection, but the value of the absorption depth is also affected by the spectral smile.

The results in fig. 11 and 12 confirm the detection of carbonate of (Ehlmann et al., 2009). We stress the fact that our approach has been applied on raw image, without stacking, neither dividing by a spectrally flat component, in contrary to published detection.

The estimated noise standard deviation is 3.5×10^{-4} from SNR but 3.4×10^{-3} using the MNF shift difference from ENVI software. The lack of fit estimated by the RMS error is 1.0×10^{-3} , in agreement with the previous two extreme values. Using the fast GPU implementation, the computation time is 20 minutes for M =600x478 pixels, $N_\lambda = 56$ bands. The computation time can can be reduced to 2.7 min without any significant change in case of a recalibration with $C\times100$.

The case of CRISM observation at a low SNR (frt0000a09) is exposed in supplementary material. No formal detection can be done because the structured noise level is higher than the signal level, with non-gaussian properties.

4.3. M^3

We propose to use the Moon Mineralogy Mapper (M^3) onboard Chandrayaan-1 image G20090209T054031 ((Pieters et al., 2009)) of Aristarchus, where peculiar olivines has been detected ((Le Mouëlic et al., 1999; Chevrel et al., 2009; Mustard et al., 2011)).

We estimate the SNR=400 from the calibration at the ground ((Green et al., 2011)),

The results in fig. 13 also confirms that the South East of Aristarchus is olivine rich but without any spectral signature of pyroxene ((Le Mouëlic et al., 1999; Chevrel et al., 2009; Mustard et al., 2011)).

The estimated noise standard deviation is 5.4×10^{-5} from SNR but 1.6×10^{-3} using the MNF shift difference from ENVI software. The lack of fit estimated by the RMS error is 2.1×10^{-4}, in agreement with the previous two extreme values. Using the fast GPU implementation, the computation time is 13 minutes for M =304x500 pixels, $N_\lambda = 56$ bands due to the very small noise level expected from the SNR (5.4×10^{-5}). The computation time can can be reduced to 1.6 min without any significant change in case of a recalibration with $C \times 100$.

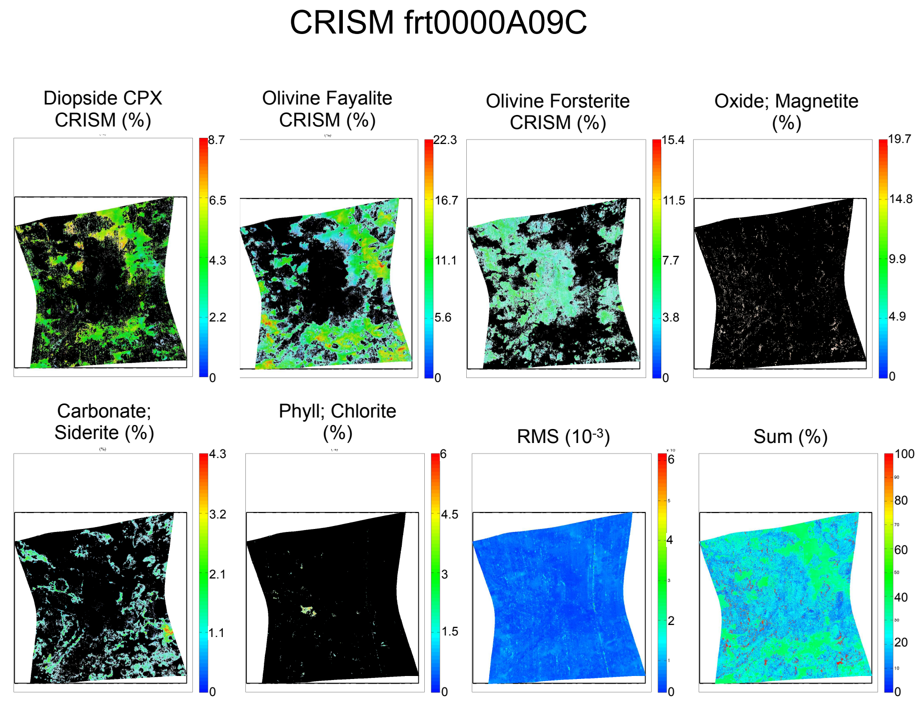

Figure 11: Detection of 6 minerals over 36 spectra on CRISM image frt0000A09C of Nili Fossae (21.3°N, 78.5°E) using IPLS in the hue-saturation-value color system. The hue (color) represents the mixing coefficient. The saturation (color or b/w) represents the error. The value (intensity of color or b/w) represents the rms. Spectral mixing coefficient map are shown with following conditions : (i) maximum mixing coefficient $> 2\%$, (ii) error on mixing coefficient $<$ mixing coefficient, and(iii) RMS $<$ 10x the dark current noise (see text). Pyroxenes, olivines, phyllosilicates and carbonate are detected and the corresponding "mixing coefficient" are mapped (color refer to the online version of the article).

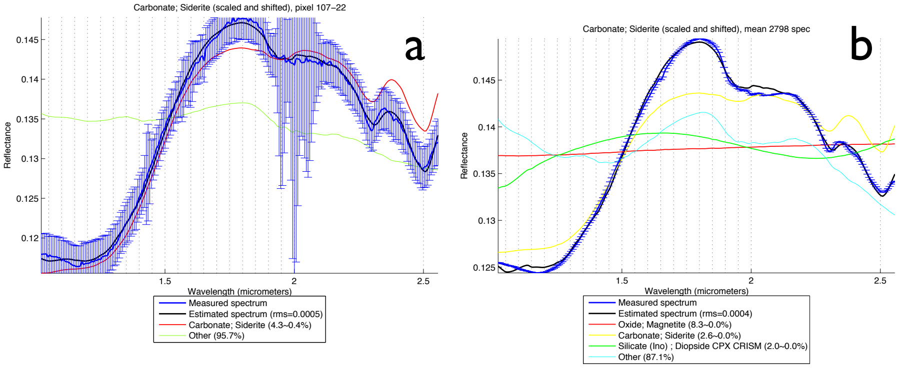

Figure 12: Example of spectra fit for the carbonate component (siderite in our spectral database). All spectral endmember with significant mixing coefficients (>2%) are plotted but the other component are retrieved by the algorithm (spectra called "Other"), mainly due to atmospheric transmission and water ice most probably in form of clouds. a) maximum mixing coefficients spectra (pixel coordinates is line No 108, row No 23), b) average value of 2896 spectra of the CRISM observation frt0000A09C.

5. Conclusion

We propose to incorporate additional spectra (constant, slope, and cosine functions) to build a new supervised algorithm, called LinMin, based on linear unmixing under positivity and sum-to-one constraints in the goal to detect minerals at the planetary surfaces. The main novelty of this approach is to treat "linearly dependent spectra" (such constant, slope and cosine functions) that create degeneracies in usual unconstrained unmixing algorithms, because under our constraints, they are not linearly dependent anymore. Usually, the reference spectra database contains linearly independent spectra (simply because they are different) so the degeneracies are very small. Nevertheless, if the reference spectra database contains significantly linearly dependent spectra, some degeneracies may occur. Adding positivity constraint significantly reduces the degeneracies. In the special case of linear subpixel mixing, the user may be interested by the most precise aerial surface proportion. In this case, once the detection step has been done, a second pass of the LinMin algorithm with the detected spectrum only can enhance the surface proportion estimation.

Some hyperspectral images may be subject to "spike" noise, with non-gaussian statistics. As stated in eq. 1, the linear unmixing methods usually assume gaussian noise, so the results may be corrupted in the worst cases. One solution may be to despike the data using average techniques ((Parente, 2008; Carter et al., 2013)) before the treatment by LinMin.

We validated the usefulness of LinMin to estimate mixing coefficients in the case of linear mixture on synthetic examples. We also tested numerically the most important non-linear effects on the detection limits : aerosols content and grain size change. Both cases are well treated with our modeling. Some minerals

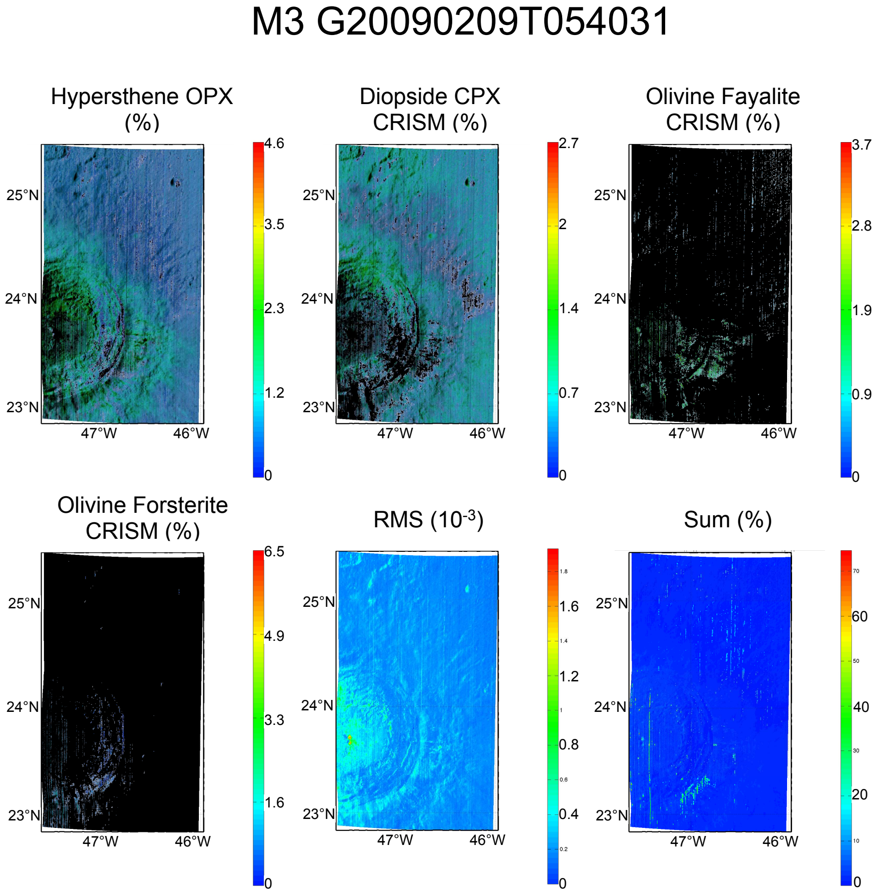

Figure 13: Detection of 4 minerals over 36 spectra on M^3 image G20090209T054031 of Aristarchus using IPLS in the hue-saturation-value color system. The hue (color) represents the mixing coefficient. The saturation (color or b/w) represents the error. The value (intensity of color or b/w) represents the rms. Spectral mixing coefficient map are shown with following conditions : (i) maximum mixing coefficient $>$ 2% , (ii) error on mixing coefficient $<$mixing coefficient, and (iii) RMS $<$ 10x the dark current noise (see text). Pyroxenes and olivines are detected and the corresponding "mixing coefficient" are mapped (color refer to the online version of the article).

with large scale feature, such olivines and pyroxenes, cannot be detected in the case of additional cosine function because their spectral signature can be also fitted with a mixture of cosine. Nevertheless, the use of additional spectra made of constant and slope components improve the detection of all minerals, including olivines and pyroxenes in comparison with no additional spectra Our approach permits to save the continuum fitting step since it is incorporated in the linear unmixing. We also showed that the knowledge of the noise covariance matrix, that can be estimated from dark current or using other techniques is important to assess the detection limits, and in particular the error on mixing coefficients.

We also tested LinMin on three real cases of hyperspectral images from OMEGA, CRISM and M^3 instruments. All three cases show detections in agreement with previous analysis, validating the LinMin with approach. The main difficulty of this approach, that is also present in band ratio and other detection method, is to optimize the threshold for detection. Nevertheless, this problem is partly tackled by the estimation of the error on the mixing coefficients. A combination of threshold on RMS residues, error on mixing coefficients, and maximum mixing coefficients seems to be the best compromise to ensure automatic detection. This strategy has to be fully validated on large dataset.

IPLS is shown to be the best numerical algorithm to solve the LinMin problem. Its fast GPU implementation is particularly relevant for the treatment of large dataset of hyperspectral images. In the future, this methodology should be applied in various planetary cases in order to study the surface geology, especially in more challenging detection situation such complex mafics and anorthosites assemblage on the Moon ((Ohtake et al., 2009)), or mixture of hydrous sulfates, hydrated acid and water ice on Europa ((McCord et al., 2010; Dalton et al., 2013)). Also a significant improvement of the mineral detection may be addressed by using spectral database adapted to the context.

Acknowledgement

We acknowledge support from the “Institut National des Sciences de l’Univers” (INSU), the “Centre National de la Recherche Scientifique” (CNRS) and “Centre National d’Etude Spatiale” (CNES) and through the ”Programme National de Planétologie”.

Appendix

Name of the 32 spectra:

1 Inosilicate (Hypersthene OPX PYX02.h ¿250u)	12 Sulfate; Gypsum	23 Carbonate; Siderite
2 Inosilicate (Diopside CPX CRISM)	13 Sulfate; Jarosite	24 Phyllosilicate (Chlorite)
3 Olivine Fayalite CRISM	14 Sulfate; Kieserite	25 Muscovite GDS116 Tanzania
4 Olivine Forsterite CRISM	15 Epsomite USGS GDS149	26 Alunite GDS83 Na63
5 Phyllosilicate (Clay Montmorillonite Bentonite)	16 Oxide; Goethite	27 Atmospheric Transmission
6 Phyllosilicate (Clay Illite Smectite)	17 Oxide; Hematite	28 H2O grain 1
7 Phyllosilicate (Serpentine Chrysotile Clinochry.)	18 Oxide; Magnetite	29 H2O grain 100
8 Phyllosilicate (Serpentine Lizardite)	19 Ferrihydrite USGS GDS75 Sy F6	30 H2O grain 1000
9 Phyllosilicate (Clay Illite)	20 Maghemite USGS GDS81 Sy (M-3)	31 CO2 grain 100
10 Phyllosilicate (Clay Kaolinite)	21 Carbonate; Calcite	32 CO2 grain 10 000
11 Phyllosilicate (Nontronite)	22 Carbonate; Dolomite	

Name of the 12 additional spectra:

33 Flat 1	37 cos 1/4	41 cos 1/2
34 Flat 0.0001	38 sin 1/4	42 sin 1/2
35 Slope Increasing	39 -cos 1/4	43 -cos 1/2
36 Slope Decreasing	40 -sin 1/4	44 -sin 1/2

References

Bibring, J.-P., Soufflot, A., Berthé, M., Langevin, Y., Gondet, B., Drossart, P., Bouyé, M., Combes, M., Puget, P., Semery, A., Bellucci, G., Formisano, V., Moroz, V., Kottsov, V., Bonello, G., Erard, S., Forni, O., Gendrin, A., Manaud, N., Poulet, F., Poulleau, G., Encrenaz, T., Fouchet, T., Melchiori, R., Altieri, F., Ignatiev, N., Titov, D., Zasova, L., Coradini, A., Capacionni, F., Cerroni, P., Fonti, S., Mangold, N., Pinet, P., Schmitt, B., Sotin, C., Hauber, E., Hoffmann, H., Jaumann, R., Keller, U., Arvidson, R., Mustard, J., Forget, F., Aug. 2004. OMEGA: Observatoire pour la Minéralogie, l'Eau, les Glaces et l'Activité. ESA SP-1240: Mars Express: the Scientific Payload, pp. 37–49.

Boardman, J., Kruse, F. A., Green, R. O., Mar. 1995. Mapping target signatures via partial unmixing of AVIRIS data: in Summaries. In: Fifth JPL Airborne Earth Science Workshop, JPL Publication 95-1. Vol. 1. pp. 23–26.

Bro, R., De Jong, S., 1997. A fast non-negativity-constrained least squares algorithm. Journal of chemometrics 11 (5), 393–401.

Carter, J., Poulet, F., Murchie, S., Bibring, J., 2013. Automated processing of planetary hyperspectral datasets for the extraction of weak mineral signatures and applications to {CRISM} observations of hydrated silicates on mars. Planetary and Space Science 76 (0), 53 – 67.
URL `http://www.sciencedirect.com/science/article/pii/S0032063312003625`

Ceamanos, X., Doute, S., 2010. Spectral smile correction of crism/mro hyperspectral images. Geoscience and Remote Sensing, IEEE Transactions on DOI - 10.1109/TGRS.2010.2064326 48 (11), 3951–3959.

Chevrel, S., Pinet, P., Daydou, Y., Le Mouëlic, S., Langevin, Y., Costard, F., Erard, S., Jan. 2009. The aristarchus plateau on the moon: Mineralogical and structural study from integrated clementine uv-vis-nir spectral data. Icarus 199 (1), 9–24.
URL `http://www.sciencedirect.com/science/article/pii/S0019103508002935`

Chevrier, V., Mathe, P., Feb. 2007. Mineralogy and evolution of the surface of mars: A review. Planetary and Space Science 55 (3), 289–314.
URL `http://www.sciencedirect.com/science/article/B6V6T-4KST3NG-4/2/57ccbb298d799322cad03ca5fedc2e26`

Chouzenoux, E., Legendre, M., Moussaoui, S., Idier, J., 2013. Fast constrained least squares spectral unmixing using primal-dual interior-point optimization. SUBMITTED TO THE IEEE JOURNAL OF SELECTED TOPICS IN APPLIED EARTH OBSERVATIONS AND REMOTE SENSING.

Chouzenoux, E., Moussaoui, S., Idier, J., Sep. 2011. Algorithme primal-dual de points interieurs pour l'estimation penalisee des cartes d'abondances en imagerie hyperspectrale. In: Actes de GRETSI 2011. Bordeaux, France, p. ID290.
URL `http://hal.archives-ouvertes.fr/hal-00625893`

Clark, R. N., Swayze, G. A., Wise, R., Livo, K. E., Hoefen, T. M., Kokaly, R. F., Sutley, S. J., 2003. Usgs digital spectral library splib05a. Tech. rep., U.S. Geological Survey.
URL `http://speclab.cr.usgs.gov/spectral-lib.html`

Combe, J.-P., Le Mouélic, S., Sotin, C., Gendrin, A., Mustard, J. F., Le Deit, L., Launeau, P., Bibring, J.-P., Gondet, B., Langevin, Y., Pinet, P., the OMEGA Science team, May 2008. Analysis of OMEGA/Mars Express data hyperspectral data using a Multiple-Endmember Linear Spectral Unmixing Model (MELSUM): Methodology and first results. Planetary and Space Science 56, 951–975.

Dalton, J. I., Cassidy, T., Paranicas, C., Shirley, J., Prockter, L., Kamp, L., Mar. 2013. Exogenic controls on sulfuric acid hydrate production at the surface of europa. Planetary and Space Science 77 (0), 45–63.
URL `http://www.sciencedirect.com/science/article/pii/S0032063312001262`

Dobigeon, N., Tourneret, J.-Y., Chang, C.-I., 2008. Semi-supervised linear spectral unmixing using a hierarchical bayesian model for hyperspectral imagery. Signal Processing, IEEE Transactions on 56 (7), 2684–2695.

Douté, S., Schmitt, B., Dec. 1998. A multilayer bidirectional reflectance model for the analysis of planetary surface hyperspectral images at visible and near-infrared wavelengths. Journal of Geophysical Research 103, 31367–31390.

Douté, S., Schmitt, B., Langevin, Y., Bibring, J.-P., Altieri, F., Bellucci, G., Gondet, B., Poulet, F., the MEX OMEGA team, Jan. 2007. South Pole of Mars: Nature and composition of the icy terrains from Mars Express OMEGA observations. Planetary and Space Science 55, 113–133.

Ehlmann, B. L., Mustard, J. F., Jun. 2012. An in-situ record of major environmental transitions on early mars at northeast syrtis major. Geophys. Res. Lett. 39 (11), L11202–.
URL `http://dx.doi.org/10.1029/2012GL051594`

Ehlmann, B. L., Mustard, J. F., Murchie, S. L., Bibring, J.-P., Meunier, A., Fraeman, A. A., Langevin, Y., Nov. 2011. Subsurface water and clay mineral formation during the early history of mars. Nature 479 (7371), 53–60.
URL `http://dx.doi.org/10.1038/nature10582`

Ehlmann, B. L., Mustard, J. F., Swayze, G. A., Clark, R. N., Bishop, J. L., Poulet, F., Des Marais, D. J., Roach, L. H., Milliken, R. E., Wray, J. J., Barnouin-Jha, O., Murchie, S. L., Oct. 2009. Identification of hydrated silicate minerals on mars using mro-crism: Geologic context near nili fossae and implications for aqueous alteration. J. Geophys. Res. 114, E00D08–.
URL `http://dx.doi.org/10.1029/2009JE003339`

Erard, S., Calvin, W., Dec. 1997. New composite spectra of mars, 0.4 microns. Icarus 130 (2), 449–460.
URL `http://www.sciencedirect.com/science/article/pii/S0019103597958309`

Erard, S., Drossart, P., Piccioni, G., Jan. 2009. Multivariate analysis of visible and infrared thermal imaging spectrometer (virtis) venus express nightside and limb observations. J. Geophys. Res. 114, –.
URL `http://dx.doi.org/10.1029/2008JE003116`

Forni, O., Poulet, F., Bibring, J.-P., Erard, S., Gomez, C., Langevin, Y., Gondet, B., The Omega Science Team, Mar. 2005. Component Separation of OMEGA Spectra with ICA. In: Mackwell, S., Stansbery, E. (Eds.), 36th Annual Lunar and Planetary Science Conference. pp. 1623–+.

Gendrin, A., Langevin, Y., Bibring, J.-P., Forni, O., Oct. 2006. A new method to investigate hyperspectral image cubes: An application of the wavelet transform. Journal of Geophysical Research (Planets) 111, 10004–+.

Gilmore, M. S., Thompson, D. R., Anderson, L. J., Karamzadeh, N., Mandrake, L., Castao, R., Jul. 2011. Superpixel segmentation for analysis of hyperspectral data sets, with application to compact reconnaissance imaging spectrometer for mars data, moon mineralogy mapper data, and ariadnes chaos, mars. J. Geophys. Res. 116 (E7), E07001–.
URL `http://dx.doi.org/10.1029/2010JE003763`

Green, R. O., Pieters, C., Mouroulis, P., Eastwood, M., Boardman, J., Glavich, T., Isaacson, P., Annadurai, M., Besse, S., Barr, D., Buratti, B., Cate, D., Chatterjee, A., Clark, R., Cheek, L., Combe, J., Dhingra, D., Essandoh, V., Geier, S., Goswami, J. N., Green, R., Haemmerle, V., Head, J., Hovland, L., Hyman, S., Klima, R., Koch, T., Kramer, G., Kumar, A. S. K., Lee, K., Lundeen, S., Malaret, E., McCord, T., McLaughlin, S., Mustard, J., Nettles, J., Petro, N., Plourde, K., Racho, C., Rodriquez, J., Runyon, C., Sellar, G., Smith, C., Sobel, H., Staid, M., Sunshine, J., Taylor, L., Thaisen, K., Tompkins, S., Tseng, H., Vane, G., Varanasi, P., White, M., Wilson, D., Oct. 2011. The moon mineralogy mapper (m3) imaging spectrometer for lunar science: Instrument description, calibration, on-orbit measurements, science data calibration and on-orbit validation. J. Geophys. Res. 116 (E10), E00G19–.
URL `http://dx.doi.org/10.1029/2011JE003797`

Heinz, D., Chein-I-Chang, 2001. Fully constrained least squares linear spectral mixture analysis method for material quantification in hyperspectral imagery. Geoscience and Remote Sensing, IEEE Transactions on 39 (3), 529–545.

Kanner, L. C., Mustard, J. F., Gendrin, A., Apr. 2007. Assessing the limits of the modified gaussian model for remote spectroscopic studies of pyroxenes on mars. Icarus 187 (2), 442–456.
URL `http://www.sciencedirect.com/science/article/B6WGF-4MK615R-3/2/38f09266a273ce0b9f2df7c7848f9515`

Kruse, F. A., Lefkoff, A. B., Boardman, J. W., Heidebrecht, K. B., Shapiro, A. T., Barloon, P. J., Goetz, A. F. H., May 1993. The spectral image processing system (sips)–interactive visualization and analysis of imaging spectrometer data. Remote Sensing of Environment 44, 145–163.

Langevin, Y., Poulet, F., Bibring, J.-P., Gondet, B., Mar. 2005. Sulfates in the North Polar Region of Mars Detected by OMEGA/Mars Express. Science 307, 1584–1586.

Lawson, C. L., Hanson, R. J., Jul. 1995. Solving Least Squares Problems. SIAM (Society for Industrial and Applied Mathematics).
URL `http://link.aip.org/link/?SIR/18/518/1`

Le Mouëlic, S., Langevin, Y., Erard, S., May 1999. The distribution of olivine in the crater aristarchus inferred from clementine nir data. Geophys. Res. Lett. 26 (9), 1195–1198.
URL `http://dx.doi.org/10.1029/1999GL900180`

McCord, T. B., Hansen, G. B., Combe, J.-P., Hayne, P., Oct. 2010. Hydrated minerals on europa's surface: An improved look from the galileo nims investigations. Icarus 209 (2), 639–650.
URL `http://www.sciencedirect.com/science/article/pii/S0019103510002186`

McGuire, P., Wolff, M., Smith, M., Arvidson, R., Murchie, S., Clancy, R., Roush, T., Cull, S., Lichtenberg, K., Wiseman, S., Green, R., Martin, T., Milliken, R., Cavender, P., Humm, D., Seelos, F., Seelos, K., Taylor, H., Ehlmann, B., Mustard, J., Pelkey, S., Titus, T., Hash, C., Malaret, E., 2008. Mro/crism retrieval of surface lambert albedos for multispectral mapping of mars with disort-based radiative transfer modeling: Phase 1; using historical climatology for temperatures, aerosol optical depths, and atmospheric pressures. Geoscience and Remote Sensing, IEEE Transactions on 46 (12), 4020–4040.

Moussaoui, S., Hauksdóttir, H., Schmidt, F., Jutten, C., Chanussot, J., Brie, D., Douté, S., Benediktsson, J., Jun. 2008. On the decomposition of mars hyperspectral data by ica and bayesian positive source separation. Neurocomputing 71 (10-12), 2194–2208.
URL `http://www.sciencedirect.com/science/article/B6V10-4RV17HX-4/1/739950d227add850ec0720718c1c2362`

Murchie, S., Arvidson, R., Bedini, P., Beisser, K., Bibring, J.-P., Bishop, J., Boldt, J., Cavender, P., Choo, T., Clancy, R. T., Darlington, E. H., Des Marais, D., Espiritu, R., Fort, D., Green, R., Guinness, E., Hayes, J., Hash, C., Heffernan, K., Hemmler, J., Heyler, G., Humm, D., Hutcheson, J., Izenberg, N., Lee, R., Lees, J., Lohr, D., Malaret, E., Martin, T., McGovern, J. A., McGuire, P., Morris, R., Mustard, J., Pelkey, S., Rhodes, E., Robinson, M., Roush, T., Schaefer, E., Seagrave, G., Seelos, F., Silverglate, P., Slavney, S., Smith, M., Shyong, W.-J., Strohbehn, K., Taylor, H., Thompson, P., Tossman, B., Wirzburger, M., Wolff, M., May 2007. Compact reconnaissance imaging spectrometer for mars (crism) on mars reconnaissance orbiter (mro). J. Geophys. Res. 112 (E5), E05S03–.
URL `http://dx.doi.org/10.1029/2006JE002682`

Mustard, J. F., Li, L., He, G., Aug. 1998. Nonlinear spectral mixture modeling of lunar multispectral data: Implications for lateral transport. Journal of Geophysical Research 103, 19419–19426.

Mustard, J. F., Pieters, C. M., Isaacson, P. J., Head, J. W., Besse, S., Clark, R. N., Klima, R. L., Petro, N. E., Staid, M. I., Sunshine, J. M., Runyon, C. J., Tompkins, S., Jun. 2011. Compositional diversity and geologic insights of the aristarchus crater from moon mineralogy mapper data. J. Geophys. Res. 116 (E6), E00G12–.
URL `http://dx.doi.org/10.1029/2010JE003726`

Mustard, J. F., Poulet, F., Gendrin, A., Bibring, J.-P., Langevin, Y., Gondet, B., Mangold, N., Bellucci, G., Altieri, F., Mar. 2005. Olivine and Pyroxene Diversity in the Crust of Mars. Science 307, 1594–1597.

Ody, A., Poulet, F., Bibring, J.-P., Loizeau, D., Carter, J., Gondet, B., Langevin, Y., Feb. 2013. Global investigation of olivine on mars: Insights

into crust and mantle compositions. J. Geophys. Res. Planets 118 (2), 234–262.
URL `http://dx.doi.org/10.1029/2012JE004149`

Ohtake, M., Matsunaga, T., Haruyama, J., Yokota, Y., Morota, T., Honda, C., Ogawa, Y., Torii, M., Miyamoto, H., Arai, T., Hirata, N., Iwasaki, A., Nakamura, R., Hiroi, T., Sugihara, T., Takeda, H., Otake, H., Pieters, C. M., Saiki, K., Kitazato, K., Abe, M., Asada, N., Demura, H., Yamaguchi, Y., Sasaki, S., Kodama, S., Terazono, J., Shirao, M., Yamaji, A., Minami, S., Akiyama, H., Josset, J.-L., Sep. 2009. The global distribution of pure anorthosite on the moon. Nature 461 (7261), 236–240.
URL `http://dx.doi.org/10.1038/nature08317`

Parente, M., Mar. 2008. A New Approach to Denoising CRISM Images. In: Lunar and Planetary Institute Science Conference Abstracts. Vol. 39 of Lunar and Planetary Institute Science Conference Abstracts. p. 2528.
URL `http://adsabs.harvard.edu/abs/2008LPI....39.2528P`

Pieters, C. M., Boardman, J., Buratti, B., Chatterjee, A., Clark, R., Glavich, T., Green, R., Head III, J., Isaacson, P., Malaret, E., et al., 2009. The moon mineralogy mapper (m3) on chandrayaan-1. Curr. Sci 96 (4), 500–505.

Poulet, F., Bibring, J.-P., Langevin, Y., Mustard, J., Mangold, N., Vincendon, M., Gondet, B., Pinet, P., Bardintzeff, J.-M., Platevoet, B., May 2009a. Quantitative compositional analysis of martian mafic regions using the mex/omega reflectance data 1. methodology, uncertainties and examples of application. Icarus 201 (1), 69–83.
URL `http://www.sciencedirect.com/science/article/B6WGF-4V8GB7J-7/2/2e4599e5853cac2cdc431481fefbbbf0`

Poulet, F., Cuzzi, J. N., Cruikshank, D. P., Roush, T., Dalle Ore, C. M., Dec. 2002. Comparison between the Shkuratov and Hapke Scattering Theories for Solid Planetary Surfaces: Application to the Surface Composition of Two Centaurs. Icarus 160, 313–324.

Poulet, F., Gomez, C., Bibring, J.-P., Langevin, Y., Gondet, B., Pinet, P., Belluci, G., Mustard, J., Jul. 2007. Martian surface mineralogy from Observatoire pour la Minéralogie, l'Eau, les Glaces et l'Activité on board the Mars Express spacecraft (OMEGA/MEx): Global mineral maps. Journal of Geophysical Research (Planets) 112, 8–+.

Poulet, F., Mangold, N., Platevoet, B., Bardintzeff, J.-M., Sautter, V., Mustard, J., Bibring, J.-P., Pinet, P., Langevin, Y., Gondet, B., Alon-Toppani, A., May 2009b. Quantitative compositional analysis of martian mafic regions using the mex/omega reflectance data: 2. petrological implications. Icarus 201 (1), 84–101.
URL `http://www.sciencedirect.com/science/article/B6WGF-4VD9X90-2/2/33d7e179b191694bac08cc430f1ddf5f`

Roberts, D., Gardner, M., Church, R., Ustin, S., Scheer, G., Green, R., Sep. 1998. Mapping chaparral in the santa monica mountains using multiple endmember spectral mixture models. Remote Sensing of Environment 65 (3), 267–279.
URL `http://www.sciencedirect.com/science/article/pii/S0034425798000376`

Schmidt, F., Bourguignon, S., Le Mouelic, S., Dobigeon, N., Theys, C., Treguier, E., 2011. Accuracy and performance of linear unmixing techniques for detecting minerals on omega/mars express. In: Hyperspectral Image and Signal Processing: Evolution in Remote Sensing (WHISPERS), 2011 3rd Workshop on DOI - 10.1109/WHISPERS.2011.6080858. pp. 1–4.

Schmidt, F., Douté, S., Schmitt, B., 2007. Wavanglet: An efficient supervised classifier for hyperspectral images. Geoscience and Remote Sensing, IEEE Transactions on 45 (5), 1374–1385.

Schmidt, F., Schmidt, A., Treguier, E., Guiheneuf, M., Moussaoui, S., Dobigeon, N., 2010. Implementation strategies for hyperspectral unmixing using bayesian source separation. Geoscience and Remote Sensing, IEEE Transactions 48 (11), 4003–4013.

Schmidt, F., Verdier, M., Legendre, M., Schmidt, A., Moussaoui, S., 2012. Accurate database for linear unmixing under constraints. In: EPSC (Madrid, 23-28 September 2012).
URL `http://meetingorganizer.copernicus.org/EPSC2012/EPSC2012-887-1.pdf`

Settle, J., Drake, N., 1993. Linear mixing and the estimation of ground cover proportions. International Journal of Remote Sensing 14 (6), 1159–1177.

Shkuratov, Y., Starukhina, L., Hoffmann, H., Arnold, G., Feb. 1999. A model of spectral albedo of particulate surfaces: Implications for optical properties of the moon. Icarus 137 (2), 235–246.
URL `http://www.sciencedirect.com/science/article/B6WGF-45GMFKB-5T/2/2b056567d27e74edbaf976c01f89d10f`

Stamnes, K., Tsay, S.-C., Jayaweera, K., Wiscombe, W., Jun. 1988. Numerically stable algorithm for discrete-ordinate-method radiative transfer in multiple scattering and emitting layered media. Appl. Opt. 27, 2502–2509.

Sunshine, J. M., Pieters, C. M., May 1993. Estimating modal abundances from the spectra of natural and laboratory pyroxene mixtures using the modified Gaussian model. Journal of Geophysical Research 98, 9075–9087.

Themelis, K. E., Rontogiannis, A. A., Koutroumbas, K. D., Feb. 2012. A Novel Hierarchical Bayesian Approach for Sparse Semisupervised Hyperspectral Unmixing. IEEE Transactions on Signal Processing 60, 585–599.

Themelis, K. E., Schmidt, F., Sykioti, O., Rontogiannis, A. A., Koutroumbas, K. D., Daglis, I. A., Aug. 2012. On the unmixing of mex/omega hyperspectral data. Planetary and Space Science 68 (1), 34–41.
URL `http://www.sciencedirect.com/science/article/pii/S0032063311003497`

Vincendon, M., 2013. Mars surface phase function constrained by orbital observations. Planetary and Space Science 76 (0), 87 – 95.
URL `http://www.sciencedirect.com/science/article/pii/S0032063312003820`

Vincendon, M., Langevin, Y., Poulet, F., Bibring, J.-P., Gondet, B., Jul. 2007. Recovery of surface reflectance spectra and evaluation of the optical depth of aerosols in the near-IR using a Monte Carlo approach: Application to the OMEGA observations of high-latitude regions of Mars. Journal of Geophysical Research (Planets) 112, 8–+.

Winter, M. E., 1999. N-findr: an algorithm for fast autonomous spectral endmember determination in hyperspectral data, 266–275.
URL `http://dx.doi.org/10.1117/12.366289`